Modification of magicity toward the dripline and its impact on electron-capture rates for stellar core collapse

Ad. R. Raduta,[1] F. Gulminelli,[2] and M. Oertel[3]
[1]*IFIN-HH, P.O. Box MG-6, Bucharest-Magurele, Romania*
[2]*CNRS/ENSICAEN/LPC/Université de Caen Basse Normandy, UMR6534, F-14050 Caen cédex, France*
[3]*LUTH, CNRS, Observatoire de Paris, Université Paris Diderot, 5 place Jules Janssen, 92195 Meudon, France*

(Received 15 October 2015; revised manuscript received 15 December 2015; published 9 February 2016)

The importance of microphysical inputs from laboratory nuclear experiments and theoretical nuclear structure calculations in the understanding of core-collapse dynamics and the subsequent supernova explosion is largely recognized in the recent literature. In this work, we analyze the impact of the masses of very neutron-rich nuclei on the matter composition during collapse and the corresponding electron-capture rate. To this end, we introduce an empirical modification of the popular Duflo-Zuker mass model to account for possible shell quenching far from stability. We study the effect of this quenching on the average electron-capture rate. We show that the pre-eminence of the closed shells with $N = 50$ and $N = 82$ in the collapse dynamics is considerably decreased if the shell gaps are reduced in the region of ^{78}Ni and beyond. As a consequence, local modifications of the overall electron-capture rate of up to 30% can be expected, depending on the strength of magicity quenching. This finding has potentially important consequences on the entropy generation, the neutrino emissivity, and the mass of the core at bounce. Our work underlines the importance of new experimental measurements in this region of the nuclear chart, the most crucial information being the nuclear mass and the Gamow-Teller strength. Reliable microscopic calculations of the associated elementary rate, in a wide range of temperatures and electron densities, optimized on these new empirical information, will be additionally needed to get quantitative predictions of the collapse dynamics.

DOI: 10.1103/PhysRevC.93.025803

I. INTRODUCTION

It is well recognized that reliable nuclear physics inputs are essential for realistic simulations of many astrophysical phenomena. Depending on the particular time scales and the resulting equilibrium conditions, this can be an equation of state (EoS) and individual (nuclear) reactions, respectively. Due to the relatively long time scale of reactions mediated by the weak interaction, the latter play an important role in many sites, for instance, the late stages of massive star evolution [1–3], thermonuclear [4,5] and core-collapse supernovae [6–8], nucleosynthesis and energy generation in x-ray bursts and other rp-process sites [9], the accreting neutron star crust [10,11], and neutron star mergers [12,13].

Within this paper, we will concentrate on core-collapse supernovae (CCSNe). Except for very low-density matter encountered in the outer layers, time scales are such that strong and electromagnetic interactions are in equilibrium. Therefore, at any time, the composition of matter can be calculated as a function of the local temperature (T), baryon number density (n_B), and proton fraction (Y_p), assuming nuclear statistical equilibrium (NSE) (see, e.g., Ref. [8]). On the contrary, weak interactions can in general not be considered in equilibrium and individual reaction rates are crucial to determine the local proton fraction. In particular, electron capture determines Y_p in the first stages of the collapse, the associated size of the homologous core, and has thus an impact on the consequent explosion dynamics [6,8,14–18].

For these simulations, the time- and space-dependent electron-capture rates are obtained for a given (n_B,T,Y_p) by folding the NSE nuclear distribution with the capture rates on individual nuclei. The microphysics uncertainties on the rates thus originate in both the uncertainties of the NSE distribution and in those associated with the individual rates.

A very complete study has recently been performed [18] on the sensitivity of core-collapse dynamics to variations of electron-capture rates in medium-heavy nuclei. The authors concentrate on the latter aspect, modifying the rates on individual nuclei according to present uncertainties, using a comprehensive set of progenitors and EoS. It was shown that important variations in the mass of the inner core at bounce and in the peak neutrino luminosity have to be expected. The variations induced by the modified electron-capture rates are five times larger than those induced by the uncertainty on the progenitor model, showing the importance of an increased reliability of nuclear physics inputs. In this same work it was clearly shown that the results are most sensitive to the region around the $N = 50$ shell closure for very neutron-rich nuclei ($74 \leqslant A \leqslant 84$).

In the present work we address the complementary aspect of uncertainties associated with the nuclear distribution. Specifically, nuclear magicity, as incorporated in mass models within currently available EoS, is known to be deeply modified in very neutron-rich nuclei [19] and the pronounced shell closures at $N = 50$ and $N = 82$ are expected to be quenched far from stability. We study here the impact of such a possible quenching on the matter composition during collapse, and the associated modification of the electron capture rate. We show that modifications of the electron capture rate of up to 30% are possible in the case of strong shell quenching.

Unlike Ref. [18], in this exploratory calculation we do not aim at computing the complete time evolution of Y_p, nor the associated modification of the inner core mass and the neutrino luminosity. Such a complete simulation would require a consistent model for the mass and electron-capture rates as determined by Fermi and Gamow-Teller transition strengths of the relevant nuclei. This is beyond the scope of the present paper. However, from general arguments and the very detailed results of Ref. [18], we expect that an increased capture rate leads to enhanced neutrino cooling, an accelerated collapse, and a higher inner core mass at bounce. The main message of the present work is to stress the need of structure information and mass measurements, particularly in the ^{78}Ni region. From the theory viewpoint, it is very important to have microscopic and consistent calculations of both masses and weak interaction rates.

The paper is organized as follows. In Sec. II the different microphysical inputs entering the electron-capture rate calculations are presented, namely the individual rates and the EoS. We show that for the latter, the mass model represents the key ingredient. The influence of the mass model on the capture rates during core collapse is discussed in Sec. III. To that end, we consider two representative collapse trajectories with typical thermodynamic conditions. An effective parametrization simulating the possible shell quenching far from stability of the two relevant shell closures $N = 50$ and $N = 82$ is introduced, and the associated modification of the global rate is discussed. Section IV contains summary and conclusions. Throughout the paper we will use units such that $k_B = 1$.

II. INGREDIENTS FOR THE CALCULATION OF THE ELECTRON-CAPTURE RATES

As mentioned above, for given thermodynamic conditions, i.e., given values of (n_B,T,Y_p), the total electron-capture rate is obtained by folding individual rates with the nuclear distribution. The latter is obtained by NSE calculations, which depend in turn on a number of inputs and in particular on the masses of different nuclei, thus on the mass model employed. In this section we detail the different ingredients entering our calculations. We will start with the individual rates in Sec. II A. The NSE model will be discussed in Sec. II B. Section II C will be devoted to the mass model and special attention will be paid to the possible quenching of magicity in very neutron-rich nuclei.

A. Individual rates

Concerning the individual rates, tabulated values are available from large-scale shell model calculations in the *sd* shell [20] and *fp* shell [21,22]. Since those calculations are still numerically very demanding, for heavier nuclei, the shell-model rates are complemented with shell-model Monte Carlo and random phase approximation (RPA) calculations [23] or an empirical approach [24]. In Ref. [25] shell-model rates on additional nuclei have been calculated; however, they are unfortunately not available as individual rates. These extended calculations still comprise a limited range of elements, masses, temperatures, and electron densities $(n_e = n_p)$ and are not sufficient to cover completely the typical conditions in the most central part of the core collapse nor the typical nuclei encountered in those situations.

We have therefore decided to use here an analytical parameterization. In the pioneering work of Ref. [26], Fuller, Fowler, and Newman have proposed such a paramaterization in the form $\lambda_{EC} = \ln 2 I_e/\langle ft\rangle_e$. I_e denotes here the space factor, depending on electron chemical potential and the reaction Q value, i.e., the energy difference between the ground states of the two participating nuclei. Nuclear structure effects enter the effective $\langle ft\rangle$ value. Following Fuller, Fowler, and Newman it is approximated by three different values, depending on the neutron and proton numbers of the parent nucleus. In particular, nuclei with $N \geqslant 40$ or $Z \leqslant 20$ are considered blocked with capture rates much reduced due to the large shell gap at $N = 40$.

Langanke *et al.* [21,22] have, among others, pointed out that correlations smear out the shell closures and that electron captures are possible on blocked nuclei, too. They have proposed an improved parametrization fitted on their detailed microscopic calculations which we will employ within our calculations. It can be written as [7]

$$\lambda_{EC} = \frac{\ln 2 \cdot \mathscr{B}}{K}\left(\frac{T}{m_e c^2}\right)^5 [F_4(\eta) - 2\chi F_3(\eta) + \chi^2 F_2(\eta)]. \quad (1)$$

with $K = 6146$ s, $\chi = (Q - \Delta E)/T$, $\eta = \chi + \mu_e/T$. T represents the temperature, and m_e and μ_e stand for electron rest mass and chemical potential, respectively. $F_i(\eta)$ denotes the relativistic Fermi integral, $F_i(\eta) = \int_0^\infty dx x^k/[1 + \exp(x - \eta)]$. $\mathscr{B}$ represents a typical (Gamow-Teller plus forbidden) matrix element. Most of the transitions do not occur between the respective ground states of the parent and daughter nucleus, but from an initial state with excitation energy E_i to a final state with excitation energy E_f. Therefore, the factor $\Delta E = E_f - E_i$ has been introduced in Eq. (1). With the values $\mathscr{B} = 4.6$ MeV and $\Delta E = 2.5$ MeV, a good agreement of the empirical expression, Eq. (1), with microscopic calculations can be achieved for a very large number of nuclei [7].

For electron-capture rates on protons we use the results of Ref. [27].

The validity of the analytic expression, Eq. (1), has been recurrently addressed in the literature (see, e.g., Refs. [7,18]) and proved to offer a fair approximation under thermodynamical conditions relevant for core collapse. Figure 1 confronts the predictions of Eq. (1), plotted as a function of the reaction Q value, with those obtained by linear interpolation of more microscopic and sophisticated weak interaction rate tables of Ref. [20] [Figs. 1(a) and 1(d)], Refs. [21,22] [Figs. 1(b) and 1(e)], and Ref. [24] [Figs. 1(c) and 1(f)]. Two representative thermodynamic conditions taken from the core-collapse trajectory of a $25M_\odot$ star in Ref. [25] are considered (see figure caption). As already evidenced by other authors, Fig. 1 shows a correct overall behavior of $\lambda_{EC}(Q)$ and, quite remarkably, it offers a fair approximation also outside the mass range for which it was designed. However, concerning individual rates, deviations can be observed. This scattering of microscopic rates around the parameterized ones were interpreted in Ref. [7] as indication that several states of parent and daughter nucleus with different transition strengths

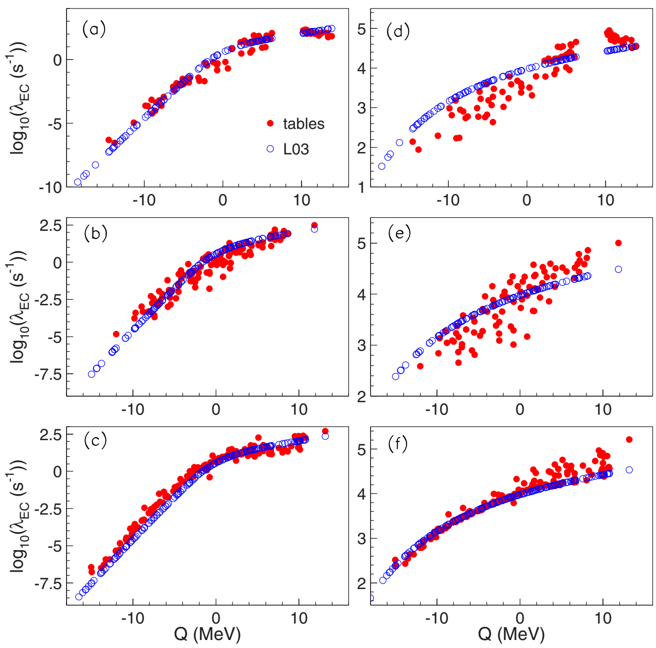

FIG. 1. Electron-capture rates: comparison between Eq. (1) (L03) (open blue circles) and interpolated values of tables from Ref. [20] ($17 \leqslant A \leqslant 39$) [panels (a) and (d)], Refs. [21,22] ($45 \leqslant A \leqslant 65$) [panels (b) and (e)], and Ref. [24] ($65 \leqslant A \leqslant 80$) [panels (c) and (f)] (solid red circles) for $T = 0.68$ MeV, $n_B = 1.32 \times 10^{-6}$ fm^{-3}, $Y_e = 0.447$ [panels (a)–(c)], and $T = 1.30$ MeV, $n_B = 1.12 \times 10^{-4}$ fm^{-3}, $Y_e = 0.361$ [panels (d)–(f)].

contribute to the same process. This effect should be less important if the electron chemical potential is sufficiently large such that electron capture becomes independent of the details of the nuclear strength distribution. Hence, at large electron densities, the scattering should be less pronounced, which can indeed be seen in Fig. 1.

These existing deviations underline the well-known fact that, in order to accurately describe astrophysical processes, it is very important to have fully microscopic calculations covering the whole mass, charge, temperature, and electron fraction domain. In this context, it was recently demonstrated in Ref. [18] that a global arbitrary rescaling of a factor 2, 3, or 10 of the unknown rates leads to important modifications of the collapse dynamics. For the purpose of the present paper, namely analyzing the influence of the extrapolation of nuclear masses into the experimentally unknown region of very neutron-rich nuclei, we tentatively stick to the extrapolation given by Eq. (1) but discuss the issue in further details in Sec. III E.

B. Extended NSE model

The model is based on a statistical distribution of compressible nuclear clusters composed by A nucleons (N neutrons and Z protons) immersed in a homogeneous background of self-interacting nucleons and electrons. The details of the model are explained elsewhere [28,29]; here we only recall the main physical ingredients which are important for the present study.

The different thermodynamic quantities in the baryonic sector are decomposed into the sum of a term pertaining to the nucleon gas and a term arising from the nuclear clusters. Let us start the discussion with the gas. In absence of clusters, it would simply be given by the free energy density of homogeneous nuclear matter at density $n_g = n_{gn} + n_{gp}$, asymmetry $\delta_g = (n_{gn} - n_{gp})/n_g$, and temperature T. In the nonrelativistic mean field approximation it reads ($q = n,p$):

$$f_{HM}(n_g,\delta_g) = \sum_q g_q \int_0^\infty \frac{dp p^2}{2\pi^2\hbar^3} n_q^T \frac{p^2}{2m_q^*} + \mathcal{E}_{\rm pot} - T s_{HM}. \tag{2}$$

The entropy density is thereby given by

$$s_{HM}(n_g,\delta_g) = -\sum_q g_q \int_0^\infty \frac{dp}{2\pi^2\hbar^3} p^2 \big[n_q^T \ln n_q^T + \big(1 - n_q^T\big) \ln \big(1 - n_q^T\big)\big]. \tag{3}$$

In these equations, $g_q = 2$ is the spin degeneracy in spin-saturated matter, n_q^T is the finite-temperature occupation number at effective chemical potential $\tilde{\mu}_q = \mu_q - \partial\mathcal{E}_{\rm pot}/\partial n_{gq}$, $n_q^T = \{1 + \exp[(p^2/2m_q^* - \tilde{\mu}_q)/T]\}^{-1}$.

The choice for the potential energy density $\mathcal{E}_{\rm pot}$ and the effective nucleon mass m_q^*, containing the interaction effects, defines the equation of state. For the applications shown in this paper we have considered a large set of different well-known Skyrme functionals for these two quantities [30], which have been successfully confronted with different nuclear structure data and are also compatible with the most recent experimental constraints on nuclear matter properties [31–33].

In the present NSE model, the free energy density of the nucleon gas is reduced with respect to the homogeneous gas expression, Eq. (2), in order to account for the finite volume occupied by the clusters [34,35] in the dense medium. The result is

$$f_g = f_{HM}\left(1 - \sum_{N,Z} n^{(N,Z)} \frac{A}{n_0(\delta)}\right). \tag{4}$$

The sum runs here over the different clusters weighted by their multiplicity per unit volume $n^{(N,Z)}$. $n_0(\delta)$ denotes the saturation density of asymmetric matter evaluated at the cluster asymmetry δ and accounts for the compressible character of the clusters. δ differs from the global asymmetry of the cluster, $(N - Z)/A$, because of Coulomb and skin effects. Within the present model, the expression for δ has been additionally modified in order to account for the influence of the external gas [28,36].

We have checked that, within these phenomenological limits, the choice of the interaction does not produce any sensible effect on our results. The reason is that the gas of unbound nucleons is very dilute and not very neutron rich under the thermodynamics conditions during collapse we are considering here, such that its energetics does not play a significant role, either for matter composition or for the total electron-capture rates. This result is perfectly compatible with previous findings [18,37].

The multiplicities of the clusters are given by the self-consistent NSE expression:

$$\ln n^{(N,Z)} = -\frac{1}{T}(F_T - \mu_B A_e - \mu_3 I_e), \quad (5)$$

where we have defined the bound fraction of clusters by $A_e = A[1 - n_g/n_0(\delta)]$, $I_e = (A_e - 2Z_e)$ and $Z_e = Z[1 - n_{pg}/n_{0p}(\delta)]$, with $n_{0p} = n_0(\delta)(1-\delta)/2$. The chemical potentials can be expressed in terms of the gas densities:

$$\mu_B \equiv \frac{\partial f_{HM}}{\partial n_g}; \quad (6)$$

$$\mu_3 \equiv \frac{\partial f_{HM}}{\partial(n_g - 2n_{gp})}. \quad (7)$$

In Eq. (5), F_T is the free energy of the cluster immersed in the nucleon gas:

$$F_T(N,Z,n_g,\delta_g) = -B - T\ln\left(A_e^{\frac{3}{2}} c_T V_{\mathrm{tot}}\right) - f_{HM}(n_g,\delta_g)\frac{A}{n_0(\delta)} + \delta F_{\mathrm{Coulomb}} + \delta F_{\mathrm{surf}}. \quad (8)$$

Here, the total volume V_{tot} has been introduced. Again, because of the low gas densities considered in this application, the third and fifth terms in Eq. (8), representing the in-medium bulk and surface modification of the free energy of the clusters due to the presence of the gas, turn out to be negligible.

The most important ingredient of the NSE model is thus the binding energy of the clusters. Its vacuum value, B, is corrected in medium by the well-known electron screening effect δF_{coul} and, to less extent, by thermal effects. The latter are described by the temperature-dependent degeneracy factor c_T,

$$c_T = \left(\frac{mT}{2\pi\hbar^2}\right)^{3/2} \int_0^{\langle S\rangle} dE[D_{N,Z}(E)\exp(-E/T)]. \quad (9)$$

$D_{N,Z}$ denotes here the density of states of the cluster, $\langle S\rangle = \min(\langle S_n\rangle,\langle S_p\rangle)$ is the average particle separation energy, and $m(= m_n = m_p)$ is the nucleon mass. For the density of states, we use a back-shifted Fermi gas model with parameters fitted to experimental data [38]. The key quantity of the model is thus the cluster binding energy, which we shall discuss in more detail in the following subsection.

C. Mass model

Consistency with the EoS of free nucleons would in principle require that the masses of the different clusters are evaluated with the energy functional employed for the gas. This is indeed the case in most recent NSE models [34,35,39,40]. However, no functional model sufficiently precisely reproduces nuclear ground states. Therefore, whenever experimentally measured nuclear masses are available, they are preferentially used in some recent NSE models [28,29,35,40]. It is also important to stress that, independent of the nuclear-matter parameters of the EoS (symmetric nuclear-matter incompressibility K_∞, symmetry energy per nucleon at the saturation density of symmetric matter J_0, slope L, and curvature K_{sym} of symmetry energy at symmetric matter saturation density), no functional model gives completely reliable extrapolations of nuclear masses in the neutron-rich region where experimental masses are not available. This leads to a model dependence of the results, which is not related to any unknown nuclear-matter parameter but rather to the poor performance of the Hartree-Fock or Thomas-Fermi approximations applied in the evaluation of nuclear masses, especially in the very neutron-rich region. Very few nuclear functional models exist, with parameters fitted with the same degree of accuracy on infinite nuclear matter and to properties of finite nuclei [41–45], and even in this case the behavior of nuclear mass towards the dripline is subject to great uncertainties.

Anyway, since in the applications considered here, the energetics of the gas plays a negligible role, the argument of consistency is not very compelling. For this reason we have chosen to employ the Duflo-Zuker mass model [46], whenever experimental measurements are missing. At present, it reproduces, within a microscopically inspired formalism, best the measured nuclear masses. For unbound nucleons, the SLy4 [47] Skyrme effective interaction is used.

In order to get an idea of the performance of the different mass models, Fig. 2 shows the evolution of the two-neutron separation energy for different elements as predicted by the 10 parameter model of Duflo and Zuker [46] and two other extremely successful and popular nuclear mass models, the Bruxelles functional BSK22 [48] and the finite-range droplet model (FRDM) by Moller and Nix [49,50], in comparison with experimental data from Ref. [51]. Since we are here mainly interested in the region around $N = 50$ and $N = 82$, elements from that region are shown. Within the different mass models, the overall dispersion on the binding energy over the global mass table[1] is 561 KeV for DZ10, 580 KeV for BSK22, and 656 KeV for FRDM [48,52].

All mass models reproduce experimental data more or less equally well. The extrapolations in the neutron-rich region, however, increasingly deviate from each other approaching the dripline. In particular, a clear and strong slope change is visible at $N = 50$ and $N = 82$ for all elements including the lightest ones for the phenomenological models DZ10 and FRDM. This indicates the presence of a very strong magic number, unmodified by the increasing neutron richness. Conversely the more microscopic BSK22 shows a more irregular behavior, and a certain quenching of magicity going towards the neutron dripline [53,54], especially for $N = 50$. This shell quenching appears to be closely related to the treatment of the residual interaction. A proper inclusion of pairing correlations is certainly a very delicate issue, but one can at least expect that it should be better treated in a self-consistent Hartree-Fock-Bogoliubov calculation such as BSK22 than in a phenomenological mass model. These differences show the difficulty of extrapolation of nuclear masses far from stability.

[1]These numbers are obtained on the more restricted AME mass table from 2003.

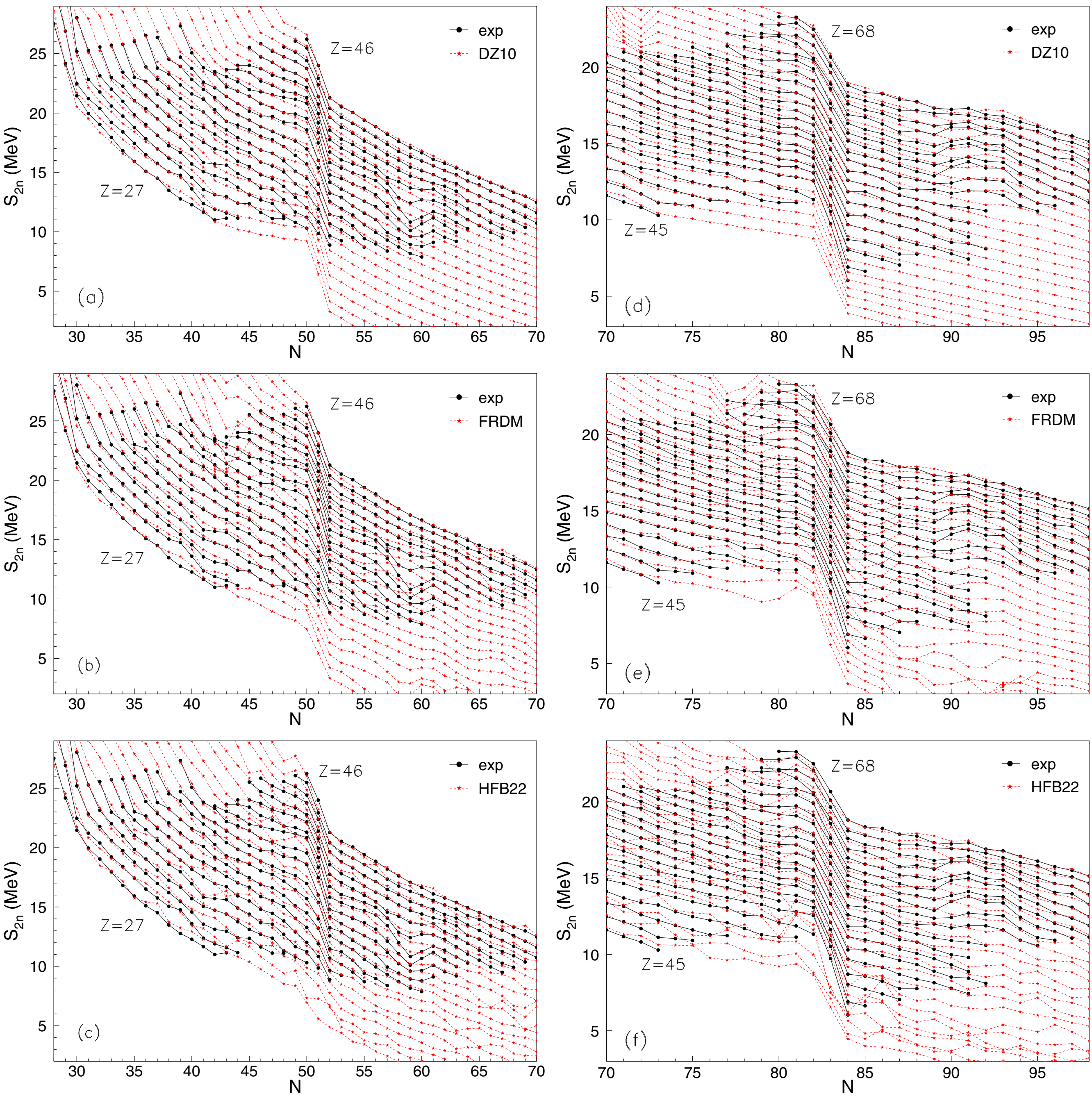

FIG. 2. Two-neutron separation energy over selected isotopic chains as predicted by different mass models (DZ10 [46], FRDM [49,50], and HFB22 [48]) (solid stars), and in comparison with experimental data (solid circles) from Ref. [51].

III. RESULTS

A. Thermodynamic conditions during core collapse

Exact values of temperature, baryon number density, and proton fraction reached during core collapse depend on many ingredients, among others, the chosen EoS and weak interaction rates. Thus, without performing a simulation, the results cannot be completely consistent. We think, however, that it is sufficient to take typical values for the purpose of the present paper, where we aim to illustrate the possible impact of a modification of nuclear masses far from stability on the electron capture rates. A detailed simulation is left for future work.

To obtain such typical values, we consider here two different core collapse trajectories from Refs. [2,6], as reported by Juodagalvis *et al.* in Ref. [25]. They correspond to the prebounce evolution for the central element of the star at an enclosed mass of 0.05 solar masses, in the case of a $15M_\odot$ and a $25M_\odot$ progenitor. These simulations use rates from tables in Refs. [21,22]. For further details on the simulations, see Ref. [2]. A more complete study would certainly require a complete and consistent simulation. We expect, however,

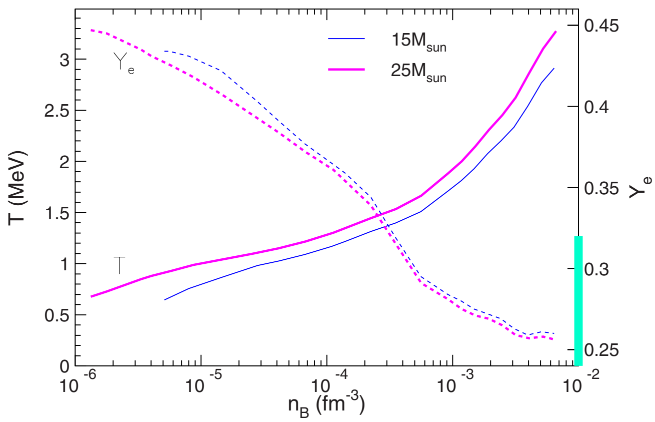

FIG. 3. Thermodynamic conditions (T, n_B, Y_e) reached by the central element in the core collapse of two progenitor stars with zero-age main sequence masses $15M_\odot$ and $25M_\odot$ as reported in Ref. [25].

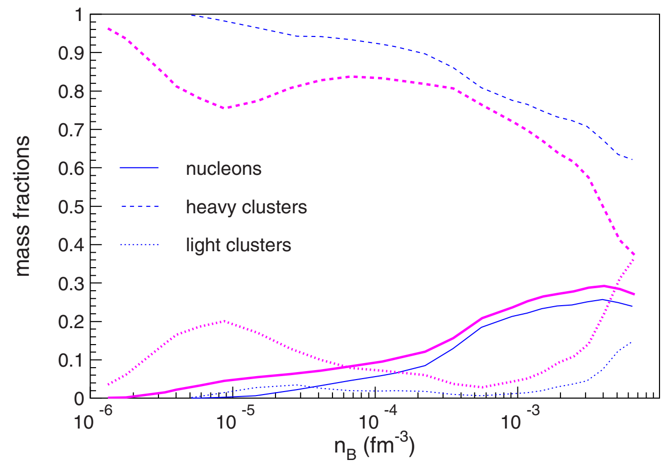

FIG. 4. Mass fractions of free nucleons and light ($2 \leqslant A < 20$) and heavy ($A \geqslant 20$) clusters obtained for the central element of the core collapse with a $15M_\odot$ (thin blue lines) and a $25M_\odot$ (thick magenta lines) progenitor; see Ref. [25]. The temporal evolution is labeled via the baryon number density as in Fig. 3. The color coding is the same as in Fig. 3.

that the qualitative findings do not depend strongly on the quantitative details. In addition, it was observed [55] that the electron fraction profiles are well correlated with the density during the collapse phase, meaning that matter, independent of the exact position inside the star, will follow similar trajectories and that our example conditions taken from the central element are valid more generally.

The thermodynamic conditions during the evolution in terms of temperature, baryon number density, and proton fraction are shown in Fig. 3. The vertical bar indicates the region in $Y_p = Y_e$, where the experimental information on nuclear masses starts to be incomplete. The nuclear abundances have thereby been obtained within our NSE model employing experimental masses [51] complemented with the DZ10 mass table [46]. For both progenitors, this happens at densities higher than $n_B \approx 4 \times 10^{-4}$ fm^{-3} and temperatures above $T \approx 1.4$ MeV. We expect thus that the mass model has a considerable influence at this stage of the collapse.

B. Chemical composition and capture rates

Using experimental masses [51] complemented with the DZ10 mass table [46], the distribution of cluster masses shows a multipeaked structure at any time during collapse and for both collapse trajectories. A first light cluster component exponentially decays up to a minimum around $A \approx 20$; then the abundances increase and, at higher masses, one or several peaks can be observed. The exact abundances and the mass numbers of the most abundant nuclei evolve with time during collapse. In order to get a global idea of these distributions, Fig. 4 displays the mass fraction corresponding to nucleons, light clusters ($2 \leqslant A < 20$), and heavier clusters ($A \geqslant 20$). The thermodynamic conditions corresponding to different times during collapse are labeled by the baryon number density. Other mass models lead to very similar results, and we will keep Duflo and Zuker [46] as our fiducial mass model in the subsequent calculations.

For the trajectory followed by the central element of the more massive progenitor, nucleons and light clusters are more abundant than for the lower mass progenitor. For the latter, heavy clusters are largely dominant during the entire evolution considered here. The reason is the systematically higher temperature obtained within the former (see Fig. 3). In addition, the abundances display a nonmonotonic behavior along the trajectory of the more massive progenitor. This is due to the interplay between the increasing temperature during collapse, which favors light clusters with respect to heavy ones, and the increasing density, which favors heavy clusters.

The composition of heavy ($A \geqslant 20$) clusters is further explored in Fig. 5. It shows the average and most probable neutron and proton numbers of heavy clusters for both trajectories. Qualitatively, similar patterns are obtained. In particular, with increasing density larger clusters are produced. At the same time, the electron fraction decreases, see Fig. 3, leading to more neutron-rich clusters. The standard deviation of the distribution of neutron and proton numbers (signaled by the vertical bars) is never negligible. This means that treating the composition of matter within the single nucleus approximation (SNA) would have produced erroneous results, as already acknowledged in the pioneering work [1].

For both trajectories, and over most of the explored density range, average N and Z numbers differ from the most probable ones. The main reason is that the distributions are not only broad but multipeaked, too. Indeed, very often the most probable nuclei lie around the $N = 50$ and $N = 82$ neutron magic numbers. Proton magic numbers are not explored because of the smaller total number of protons. The reduced number of protons with respect to neutrons explains also the systematically narrower distributions in Z. Finally, the increasing width of the distributions in neutron number with increasing density is due to the competition between the two magic numbers.

In Ref. [18], very similar multiplicity distributions have been obtained for a bunch of different trajectories with different progenitor models and EoS. We therefore conclude

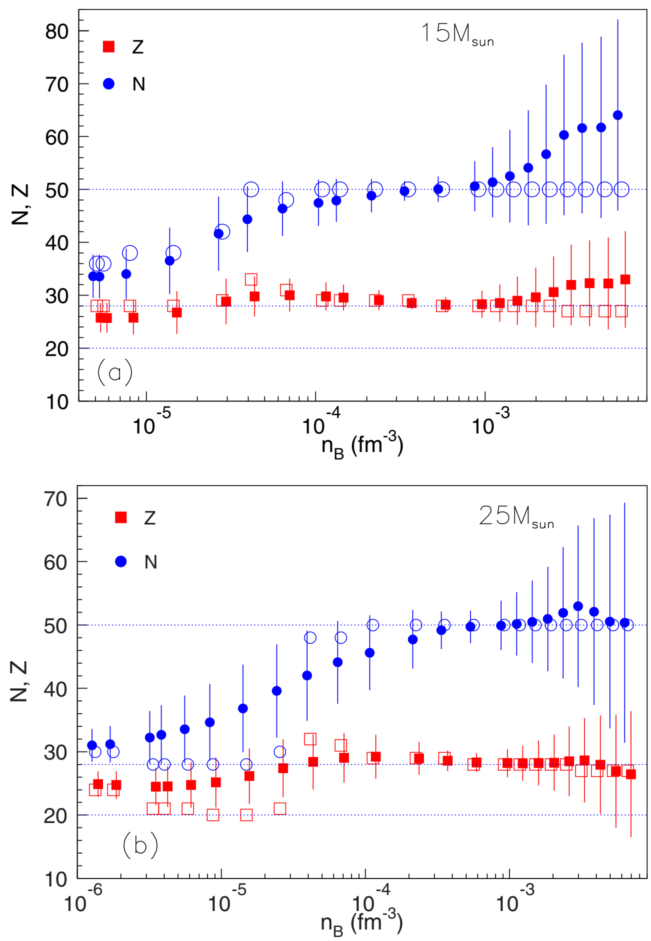

FIG. 5. Average (solid symbols) and most probable (open symbols) proton and neutron numbers of heavy ($A \geqslant 20$) nuclei produced in the central element of the core-collapsing $15M_{\odot}$ and $25M_{\odot}$ progenitors [25] as a function of baryonic density. The vertical bars correspond to the standard deviation of the distribution. For better readability, N and Z data have been slightly displaced in density.

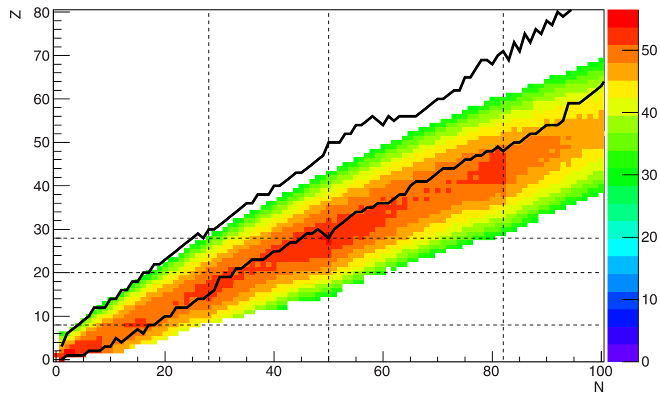

FIG. 6. Nuclear abundances (arbitrary units) corresponding to $n_B = 1.18 \times 10^{-3}$ fm^{-3}, $T = 2$ MeV, $Y_e = 0.275$. The solid lines mark the boundaries of experimental mass measurements. The dotted lines mark magic numbers.

that the present thermodynamic conditions are reasonably representative of the generic evolution of the central element.

To better understand the origin of this behavior, Fig. 6 displays the isotopic abundances corresponding to $n_B = 1.18 \times 10^{-3}$ fm^{-3}, $T = 2$ MeV, $Y_e = 0.275$, i.e., at the time where the dispersion of the distribution of Fig. 5 starts to become non-negligible. The distribution is centered around the $N = 50$ neutron magic number, and the important width is due to the emergence of a second peak around $N = 82$. This finding is in agreement with the simulations in Ref. [18] and a similar effect was observed for the neutron star crust in Refs. [56,57]. In particular, in Ref. [18] it was shown that the overall variation of the electron fraction during the collapse is most sensitive to the electron-capture rate on nuclei in the mass range $74 \leqslant A \leqslant 84$, particularly on ^{78}Ni, ^{79}Cu, and ^{79}Zn close to the $N = 50$ shell closure. Our findings confirm these results. The two lines in Fig. 6 show the borders of the region where mass measurements exist, though with a variable degree of precision. We can see that the most abundant nuclei lay just outside this border. This means that their abundance, and therefore their pre-eminent role in the electron capture mechanism, relies on the extrapolation of the $N = 50$ and $N = 82$ shell closure far from stability, in a neutron-rich region where mass measurements do not exist and spectroscopic information is scarce and incomplete. This means that small modifications in the nuclear binding energies of nuclei with masses not yet measured, but measurable in a near future, can change star matter composition and, consequently, all astrophysical quantities depending on it, notably weak rates. This point will be explored in more detail in the following subsection.

For this fiducial model, we now show the NSE averaged electron-capture (EC) rates on the different species $\mathscr{C}$, $\langle \lambda_{EC}^{\mathscr{C}} \rangle = \sum_{(N,Z)\in\mathscr{C}} n^{(N,Z)} \lambda_{EC}^{(N,Z)} / \sum_{N,Z} n^{(N,Z)}$. The two above-mentioned core-collapse trajectories will be considered and L03 formulas (see Sec. II A) will be used. Let us first concentrate on the capture rates on heavy nuclei. As is well known [1], a huge number of different nuclear species contribute to the total rate in all thermodynamics conditions. This can be appreciated by limiting the rate calculation to the N most probable nuclei, $\langle \lambda_{EC}^{N} \rangle = \sum_{i=1}^{N} n_i \lambda_{EC}^{i} / \sum_{N,Z} n^{(N,Z)}$, where n_i is the abundance of the ith most probable cluster. Comparing the result obtained with $N = 30$ and $N = 60$ with the one corresponding to the whole distribution, one can see how important it is to properly account for the complete distribution of nuclear species. In the case of both progenitors, the 60 most probable nuclei never exhaust the average electron-capture rate on heavy nuclei and, for instance, at $n_B = 1.4 \times 10^{-5}$ fm^{-3} they account for only 60% of $\langle \lambda_{EC}^{\mathrm{heavy}} \rangle$.

The inadequacy of the single-nucleus approximation was recently stressed in Ref. [16]. In that work it was shown that sizable differences in the collapse dynamics are obtained if the NSE model is replaced with a more conventional model [58] considering a single representative Wigner-Seitz cell for each thermodynamic condition, even if the same TM1 energy functional was employed in both models. However, in that work the individual rates were replaced by a single rate on the most probable cluster, using the simplified Bruenn parametrization [15].

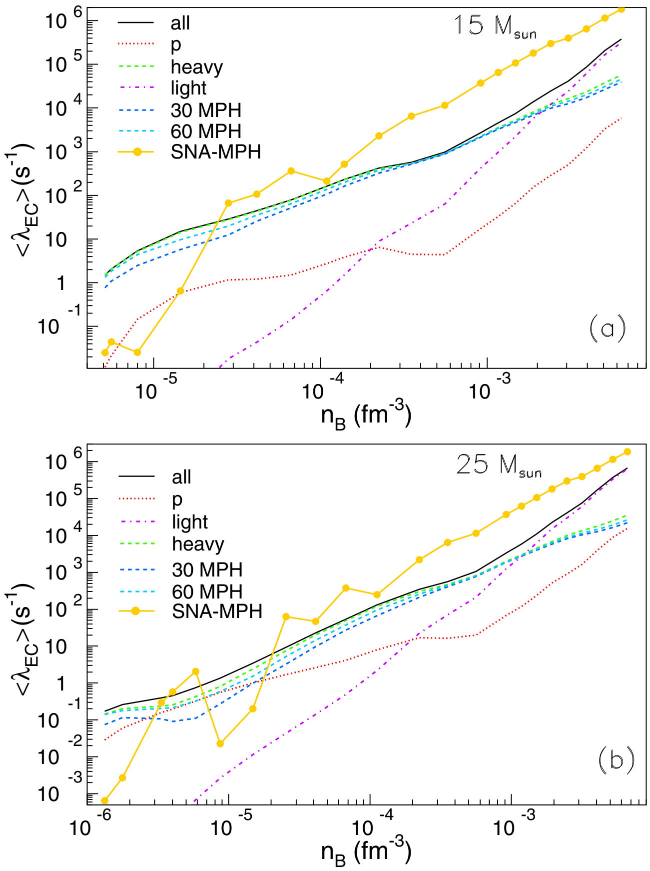

FIG. 7. Average electron-capture (EC) rates on protons, light ($2 \leqslant A < 20$) nuclei, heavy ($A \geqslant 20$) nuclei, and the 30 (dashed blue lines) and 60 (dashed cyan lines) most probable heavy nuclei. SNA-like EC rates (see text) are also plotted (SNA-MPH). The considered thermodynamical trajectories correspond to the central mass element of the $15 M_\odot$ and $25 M_\odot$ progenitors [25].

Our results show that the complete nuclear distribution should also be used in the calculation of the rates. If we replace the folding of the individual rates with the electron-capture rate of the most probable nucleus weighted by the baryon number fraction bound in clusters, $\langle \lambda_{EC}^{SNA} \rangle = (n_{cl}/n_B)\lambda_{EC}^{MP}$, the result (lines with points) is seen to very badly reproduce the complete folding result. As one may see in Fig. 7, at low densities $\langle \lambda_{EC}^{SNA} \rangle$ generally underestimates the NSE averaged electron-capture rate. In addition, due to structure effects related to the low temperatures at these densities, it manifests a huge scattering. On the contrary, at higher densities and temperatures ($n_B > 3 \times 10^{-5}$ fm^{-3}), $\langle \lambda_{EC}^{SNA} \rangle$ largely overestimates the NSE-averaged electron capture rate. Obviously, different values are expected if instead of the L03 approximation, other prescriptions are employed for the individual electron-capture rates; see the discussion in Ref. [18], too. However, the general trend induced by the different averaging procedures should remain the same.

Concerning the electron-capture rates on light nuclei, they are negligible at the beginning of the collapse but increase strongly, mainly due to the increasing temperature, and become dominant in the latest stage. This underlines the importance of including microscopic calculation of electron-capture rates for light nuclei, too [59].

The total rates are given by the sum of the different contributions, including electron capture on free protons (dotted lines), which, however, plays a minor role at all times considered here. Comparing Figs. 3, 5, and 7, we note that for thermodynamic conditions where very neutron-rich nuclei start to dominate, with masses which are not experimentally known, they still represent the major electron-capture source. This qualitative picture is independent of the progenitor mass. From a more quantitative point of view, the relative importance of heavy clusters is higher for the lower mass progenitor, essentially because of the lower temperatures reached during the collapse.

C. Evolution of magicity far from stability

It is well known in the recent nuclear structure literature that even major shell closures can be quenched far from stability; see, e.g., [19,60,61]. Very clear evidence exists for the $N = 20$ magic number [19,60], which corresponds to a huge gap for decreasing proton number up to ^{34}Si, and suddenly disappears in the next even-even isotope ^{32}Mg. This is partly due to the modification of single-particle energies far from stability, with the consequence that new magic numbers can appear corresponding to strongly deformed configurations. However, the main reason for the modification of magicity relies on effects which go beyond the naive single-particle shell model. First, the effect of the proton-neutron residual interaction in nuclei with strong asymmetry is decreased; second, correlations play an increasing role which makes the very concept of shell closure less relevant. As a consequence, the main effect is a quenching of the shell gap, even if secondary new gaps can appear in very localized regions of the nuclear chart.

The possible modification of the $N = 50$ and $N = 82$ shell gaps far from stability is the object of intense theoretical and experimental research in nuclear structure (e.g., [19,61]). Here, we do not have the ambition to model this phenomenon but simply analyze the modifications in the matter composition and associated electron-capture rates, which would be induced by the expected shell quenching.

A similar idea was proposed in Ref. [62], who showed that a modified mass formula built to incorporate the possibility of shell quenching has a striking impact on canonical calculations of the r-process. We follow a similar strategy as in Ref. [62] and introduce a modified expression for the binding energy in the following form:

$$B^m(A,Z) \begin{cases} = B^{\exp}(A,Z), & Z_i^{\exp}(A) \leqslant Z \leqslant Z_s^{\exp}(A) \\ = B^{LD}(A,Z) + f\left(Z_i^{\exp}(A) - Z, \Delta Z, \alpha\right)(B^{DZ}(A,Z) - B^{LD}(A,Z)), & Z_i^{DZ}(A) \leqslant Z < Z_i^{\exp}(A) \\ = B^{LD}(A,Z) + f\left(Z - Z_s^{\exp}(A), \Delta Z, \alpha\right)(B^{DZ}(A,Z) - B^{LD}(A,Z)), & Z_s^{\exp}(A) < Z \leqslant Z_s^{DZ}(A), \end{cases} \quad (10)$$

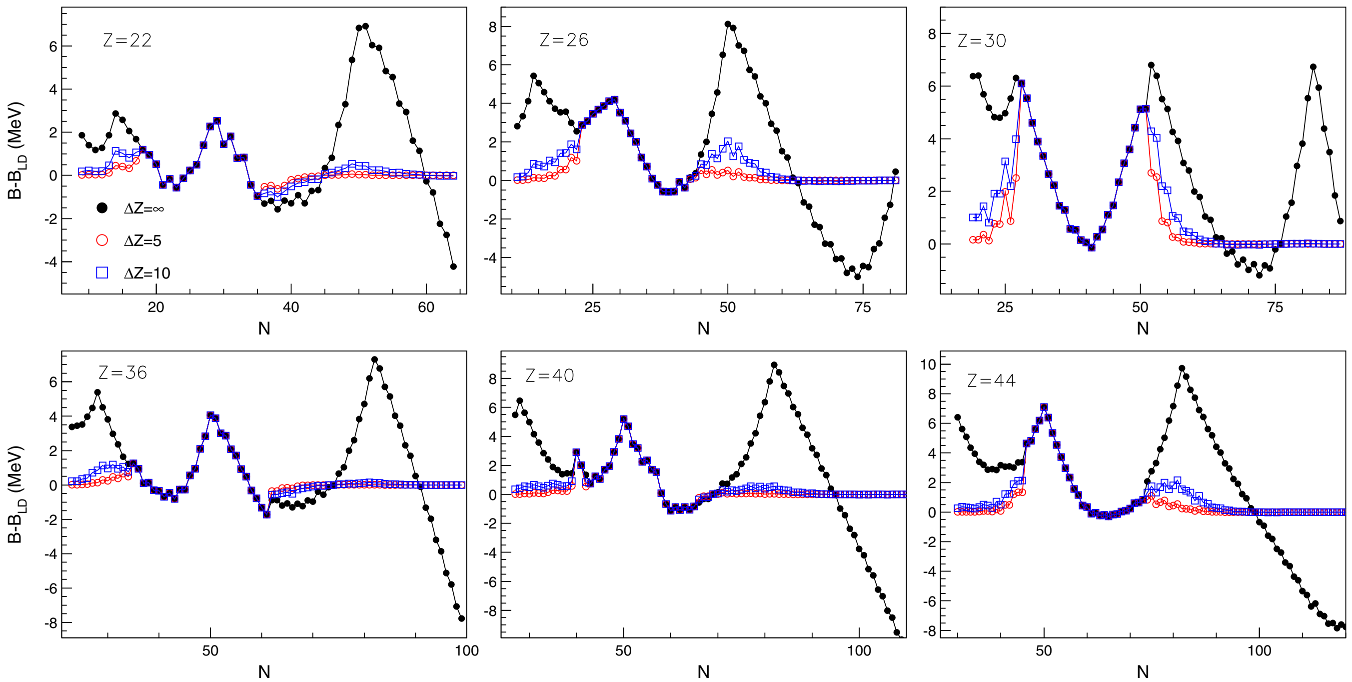

FIG. 8. LDM-shifted binding energy as a function of neutron number for different isotopes strongly populated during core collapse. DZ10 [46] results (solid black dots) are plotted along modified results B^m corresponding to two different scenarios of shell quenching (see text for details).

where $B^{\exp}(A,Z)$ and $B^{DZ}(A,Z)$ stand for the experimental binding energy [51] and predictions of DZ10 mass model [46], respectively. $Z_i^{\exp}(A)$ (resp., $Z_i^{DZ}(A)$) and $Z_s^{\exp}(A)$ (resp., $Z_s^{DZ}(A)$) correspond to the most neutron-rich and, respectively, most neutron-poor nucleus with A nucleons for which experimental masses (resp., predictions of DZ10) exist. $B^{LD}(A,Z)$ is a simple liquid-drop binding energy calculated according to

$$\begin{aligned} B^{LD}(A,Z) = {} & a_v A - a_s A^{2/3} - a_{vi} 4I(I+1)/A \\ & + a_{si} 4I(I+1)/A^{4/3} - a_c Z(Z-1)/A^{1/3} \\ & + V_p(A,Z), \end{aligned} \tag{11}$$

with $I = |A-2Z|/2$, $a_v = 15.62$ MeV, $a_s = 17.8$ MeV, $a_{vi} = 29$ MeV, $a_{si} = 38.5$ MeV, $a_c = 0.7$ MeV, and $V_p = \pm 12/\sqrt{A}$ MeV for even-even (+) and, respectively, odd-odd nuclei (−).

Finally we introduce a smearing function depending on the parameters ΔZ and $\alpha < 0$ which determine how sudden the shell quenching is supposed to be:

$$f(x,\Delta Z,\alpha) = \exp[\alpha x/\Delta Z]. \tag{12}$$

Small values of ΔZ correspond to maximum quenching, while in the limit $\Delta Z \to \infty$ we recover the DZ10 functional form, which predicts preserved magic numbers up to the dripline.

The impact of the shell quenching following Eq. (10) on the binding energy is illustrated in Fig. 8 for different arbitrary values of the smearing parameter $\Delta Z = 5,10,\infty$ and $\alpha = \log(10^{-2})$. Different clusters are displayed as a function of neutron number. These elements have been chosen since they are strongly populated in the later phase of the collapse.

As observed before, the DZ10 model shows a pronounced shell closure at $N = 50$ and $N = 82$ for all elements including the exotic ones like ^{72}Ti and ^{118}Kr. In the modified expression, Eq. (10), the gap is quenched far from stability, and the quenching is more or less pronounced depending on the choice of the parameter ΔZ.

The effect of the modification of the mass formula on the distribution of nuclei is shown in Fig. 9 for three different representative conditions during the collapse, taken from the $25M_\odot$ progenitor [25]. Obviously, the effect of shell quenching is to reduce the size of the magic peaks and favor open shell nuclei, thus leading to a wider isotopic distribution.

D. Effect on the electron capture rates

Our final result about the impact of shell quenching towards the dripline on NSE-averaged electron capture rate is shown in Fig. 10. The different predictions are plotted in terms of relative deviations with respect to the fiducial model. The strength of the quenching of magicity has thereby been varied considering different values of the parameters $\Delta Z = 2,5,10$ and $\alpha = \log(10^{-2})$ and the results are shown for the trajectories followed by the two different progenitors. Figure 10(a) shows the NSE-averaged electron capture rates on heavy nuclei. A similar pattern is obtained for both trajectories and for all considered shell-quenching scenarios. When neutron-rich nuclei start to become abundant, shell quenching first leads to an increased electron-capture rate. The reason is that nonmagic nuclei become significantly more abundant and the

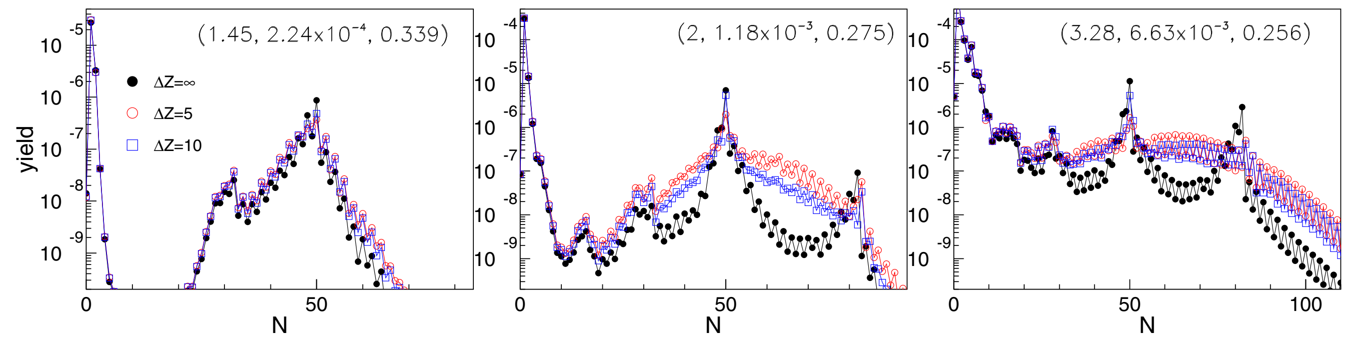

FIG. 9. Impact of nuclear binding energies on nuclear abundances: the distribution of clusters with a given neutron number is shown. The considered thermodynamic conditions (T [MeV], n_B [fm^{-3}], Y_p) are mentioned on each panel, corresponding to three different times in the evolution of the central element of the collapse with a 25 $M_\odot$ progenitor [25]. The same prescriptions for the binding energies as in Fig. 8 are used.

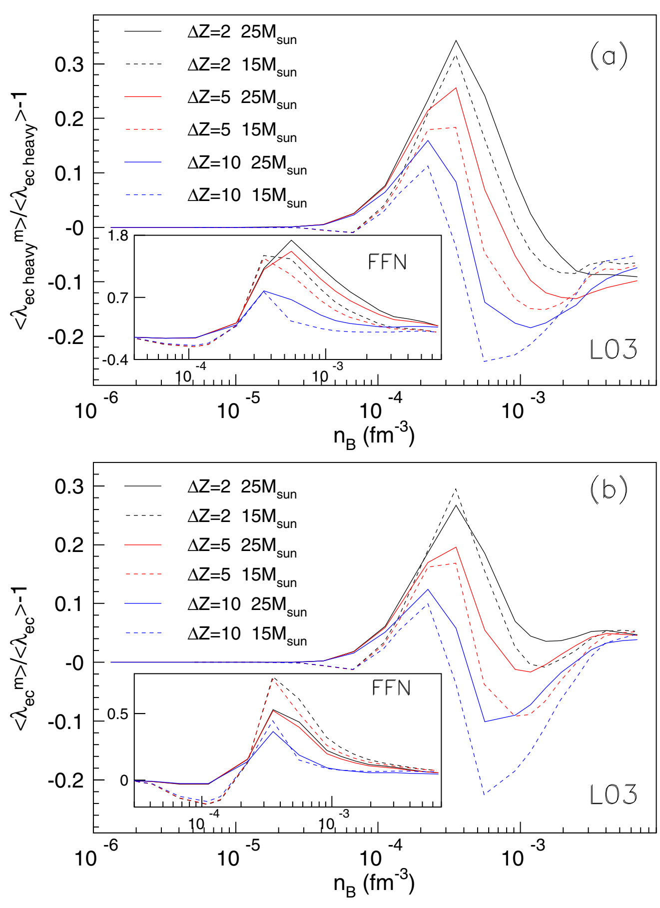

FIG. 10. Ratio between NSE-averaged electron capture rates using the shell-quenched mass functional (see text) and the original DZ10 [46] mass model. The thermodynamic conditions are taken from the two core-collapse trajectories of the central element of a $15M_\odot$ (dashed lines) and a $25M_\odot$ (full lines) progenitor [25]. The temporal evolution is labeled by the baryon number density as before. The averaged rate is calculated only on heavy nuclei ($A \geqslant 20$) in the upper panel and on all nuclei in the lower panel. Different quenching factors ΔZ are considered (see text). For individual electron-capture rates Eq. (1) (predictions of Ref. [26]) are considered in the main frames (inserts).

abundance of $N = 50$ magic nuclei decreases slightly. In this regime shell quenching on the electron-capture rates on heavy nuclei is more pronounced, and lasts for a longer time, in the case of the $25M_\odot$ progenitor. Towards the end of the considered trajectories, the opposite effect is observed. Here shell quenching is responsible for a reduction of one order of magnitude in the abundance of $N = 50$ and $N = 82$ magic nuclei, not compensated by the increase in the abundance of nonmagic nuclei and the corresponding increase in the Q value. In the two regimes, the amplitude of the effect depends on both, the quenching parameter ΔZ, and the progenitor mass. It may amount up to 30%. Figure 10(b) shows that, despite the fact that heavy nuclei represent only a fraction of the whole mass and more isospin-symmetric light nuclei are not affected by shell quenching, the modification of the electron-capture rate on heavy nuclei still impacts the inclusive rate up to $n_B \lesssim 3 \times 10^{-4}$ fm^{-3}, where $X_{\text{heavy}} \gtrsim 0.8$ (see Fig. 4), $\langle \lambda_{EC}^m \rangle / \langle \lambda_{EC} \rangle \approx \langle \lambda_{EC}^{m\text{heavy}} \rangle / \langle \lambda_{EC}^{\text{heavy}} \rangle$. For the highest considered densities the overall modification of electron-capture rates is the opposite of that seen for heavy clusters. More precisely, shell quenching here points toward an increase of electron capture. This happens because light clusters are favorably produced.

E. Shell quenching and individual rates

In the discussion of Sec. III D we have considered that the individual capture rates are conveniently described by Eq. (1) also in the extreme neutron-rich case around $N = 50$ and $N = 82$. However, in that region Eq. (1) does not any more represent a fit of microscopic estimations, but only an extrapolation. Recent large-scale shell-model calculations for r-process waiting point nuclei [63], including the $0g_{9/2}$ neutron orbit in the valence space and employing matrix elements optimized on the neutron-rich Ni isotopic chain [64], obtain a much steeper decrease of the decay half-lives with the proton number at $N = 50$, and an overall improved agreement with experimental data, with respect to the previous SM calculation used to benchmark Eq. (1). On more general grounds, the rates reflect the fragmentation of the Gamow-Teller strength which, in turn, originates from the fragmentation of the single-particle states in the daughter nucleus due to correlations. These same correlations are known to be responsible for magicity quenching in neutron-rich nuclei [19], meaning that the rates and the mass model are closely linked. Specifically, in the extreme independent particle model, where magic numbers are preserved over the nuclear chart, GT transitions in nuclei with $N > 40$ are Pauli blocked in the ground state. In that simplified picture the capture probability can take place only due to finite temperature effects, and is therefore strongly reduced [15]. Dedicated QRPA calculations [65] are in progress to achieve the aim of a consistent calculation of the individual electron-capture probabilities together with the mass model and the energy functional describing the self-interaction of unbound particles. This ambitious project is beyond the purpose of the present paper. However, to give a flavor of the sensitivity of the NSE-averaged electron-capture rates on individual electron capture rates, we have also performed calculations using, instead of Eq. (1), the analytical formula proposed in Ref. [26], which is based on the single-particle picture for the GT transition (FFN). The inserts in Figs. 10(a) and 10(b) show the corresponding results. Several differences are to be noted with respect to the previous results. First, the evolution as a function of density is qualitatively different. Then, the consequences of shell quenching appear to be much more important, especially when electron capture on heavy nuclei is analyzed. They may reach 180%.

IV. SUMMARY AND CONCLUSIONS

In this paper we have examined the consequence of a possible quenching of the $N = 50$ and $N = 82$ shell closures on the electron-capture rates during core collapse. As basis of the analysis, we have considered the same typical thermodynamic conditions as in Ref. [25]. They correspond to the prebounce evolution of the central element of the star obtained within a core-collapse simulation using two different progenitors, a $15M_\odot$ and a $25M_\odot$ one, from Refs. [2]. In agreement with Ref. [18] we find that the properties of very exotic nuclei around these two shell closures is a key microscopic information to predict the evolution of the electron fraction during collapse.

We have pointed out that a possible quenching of these shell closures considerably affects the nuclear distribution and consequently the electron-capture rates during collapse. Using the parametrization of Ref. [7], Eq. (1), for the rates on individual nuclei, we have analyzed the modification of NSE average electron-capture rates for different scenarios of shell quenching. Depending on the progenitor mass and the importance of shell quenching, modifications of the electron capture rates of up to 30% have been obtained. An effect even stronger would be obtained if the unblocking effect of $N > 40$ nuclei of Ref. [7] is overestimated far from stability, as it seems to be suggested by the recent large-scale shell-model calculations of Ref. [63]. We expect that such effects, once consistently included in the time-dependent evolution of the collapse, have a sizable effect on neutrino emissivity and on the enclosed mass at bounce.

In this work the quenching effect is governed by the parameter ΔZ whose value is chosen in an arbitrary way. More sophisticated calculations in microscopic theories, such as modern interaction configuration shell-model calculations in the relevant nuclear chart region [66], are currently under way, and will give essential information on the effective importance of the shell quenching. However, the last word will be clearly given by phenomenology. New precise mass measurements at the edges of the known isotopic table could allow for a much better extrapolation towards the neutron-rich region in the very near future.

Finally, it is important to stress that the modification of nuclear structure far from stability is expected to influence not only the nuclear mass, but also the individual electron-capture probabilities, which should be consistently calculated together with the mass model and the energy functional describing the self-interaction of unbound particles.

ACKNOWLEDGMENTS

This work has been partially funded by the SN2NS Project ANR-10-BLAN-0503 and by NewCompstar, COST Action MP1304. A.R.R. acknowledges partial support from the Romanian National Authority for Scientific Research under Grants No. PN-II-ID-PCE-2011-3-0092 and No. PN 09 37 01 05 and kind hospitality from LPC-Caen and LUTH-Meudon.

[1] M. B. Aufderheide, I. Fushiki, S. E. Woosley, and D. A. Hartmann, Astrophys. Journ. Suppl. **91**, 389 (1994).
[2] A. Heger, K. Langanke, G. Martinez-Pinedo, and S. E. Woosley, Phys. Rev. Lett. **86**, 1678 (2001); A. Heger, S. E. Woosley, G. Martinez-Pinedo, and K. Langanke, Astrophys. J. **560**, 307 (2001).
[3] G. Martinez-Pinedo, Y. H. Lam, K. Langanke, R. G. T. Zegers, and C. Sullivan, Phys. Rev. C **89**, 045806 (2014).
[4] K. Iwamoto, F. Brachwitz, K. Nomoto *et al.*, Astrophys. J. Suppl. **125**, 439 (1999).
[5] F. Brachwitz *et al.*, Astrophys. J. **536**, 934 (2000).
[6] W. R. Hix, O. E. B. Messer, A. Mezzacappa, M. Liebendörfer, J. Sampaio, K. Langanke, D. J. Dean, and G. Martinez-Pinedo, Phys. Rev. Lett. **91**, 201102 (2003).
[7] K. Langanke, G. Martínez-Pinedo, J. M. Sampaio, D. J. Dean, W. R. Hix, O. E. B. Messer, A. Mezzacappa, M. Liebendörfer, H.-Th. Janka, and M. Rampp, Phys. Rev. Lett. **90**, 241102 (2003); K. Langanke and G. Martinez-Pinedo, Rev. Mod. Phys. **75**, 819 (2003).
[8] H. T. Janka, K. Langanke, A. Marek, G. Martinez-Pinedo, and B. Mueller, Phys. Rep. **442**, 38 (2007).
[9] H. Schatz, A. Aprahamian, J. Gorres, M. Wiescher, T. Rauscher, J. F. Rembges, F.-K. Thielemann, B. Pfeiffer, P. Moller, K.-L. Kratz, H. Herndl, B. A. Brown, and H. Rebel, Phys. Rep. **294**, 167 (1998).
[10] S. Gupta, E. F. Brown, H. Schatz, P. Moeller, and K. L. Kratz, Astrophys. J. **662**, 1188 (2007).
[11] H. Schatz *et al.*, Nature (London) **505**, 62 (2014).
[12] J. J. Mendoza-Temis, G. Martinez-Pinedo, K. Langanke, A. Bauswein, and H. T. Janka, Phys. Rev. C **92**, 055805 (2015).
[13] S. Goriely, A. Bauswein, O. Just, E. Pllumbi, and H. T. Janka, Mon. Not. Roy. Astron. Soc. **452**, 3894 (2015).

[14] H. A. Bethe, G. E. Brown, J. Applegate, and J. M. Lattimer, Nucl. Phys. A **324**, 487 (1979).
[15] S. W. Bruenn, Astrophys. J. Suppl. **58**, 771 (1985).
[16] M. Hempel, T. Fischer, J. Schaffner-Bielich, and M. Liebendorfer, Astrophys. J. **748**, 70 (2012).
[17] K. Langanke and G. Martinez-Pinedo, Nucl. Phys. A **928**, 305 (2014).
[18] C. Sullivan, E. O'Connor, R. G. T. Zegers, T. Grubb, and S. A. Austin, Astrophys. J. **816**, 44 (2016).
[19] O. Sorlin and M. G. Porquet, Prog. Part. Nucl. Phys. **61**, 602 (2008).
[20] T. Oda, M. Hino, K. Muto, M. Takahara, and K. Sato, At. Data Nucl. Data Tables **56**, 231 (1994).
[21] K. Langanke and G. Martinez-Pinedo, Nucl. Phys. A **673**, 481 (2000).
[22] K. Langanke and G. Martinez-Pinedo, At. Data Nucl. Data Tables **79**, 1 (2001).
[23] J.-U. Nabi and H. V. Klapdor-Kleingrothaus, At. Data Nucl. Data Tables **88**, 237476 (2004).
[24] J. Pruet and G. M. Fuller, Astrophys. J. Suppl. Ser. **149**, 189 (2003).
[25] A. Juodagalvis, K. Langanke, W. R. Hix, G. Martnez-Pinedo, J. M. Sampaio, Nucl. Phys. A **848**, 454 (2010).
[26] G. M. Fowler, W. A. Fuller, and M. J. Newman, Astrophys. J. **293**, 1 (1985).
[27] G. M. Fowler, W. A. Fuller, and M. J. Newman, Astrophy. J. Suppl. **48**, 279 (1982).
[28] F. Gulminelli and Ad. R. Raduta, Phys. Rev. C **92**, 055803 (2015).
[29] S. Burrello, F. Gulminelli, F. Aymard, M. Colonna, and Ad. R. Raduta, Phys. Rev. C **92**, 055804 (2015).
[30] P. Danielewicz and J. Lee, Nucl. Phys. A **818**, 36 (2009).
[31] M. B. Tsang, J. R. Stone, F. Camera, P. Danielewicz, S. Gandolfi, K. Hebeler, C. J. Horowitz, Jenny Lee, W. G. Lynch, Z. Kohley, R. Lemmon, P. Möller, T. Murakami, S. Riordan, X. Roca-Maza, F. Sammarruca, A. W. Steiner, I. Vidaña, and S. J. Yennello, Phys. Rev. C **86**, 015803 (2012).
[32] J. M. Lattimer and Y. Lim, Astrophys. J. **771**, 51 (2013).
[33] J. M. Lattimer and A. W. Steiner, Eur. Phys. J. A **50**, 40 (2014).
[34] Ad. R. Raduta and F. Gulminelli, Phys. Rev. C **82**, 065801 (2010).
[35] M. Hempel and J. Schaffner-Bielich, Nucl. Phys. A **837**, 210 (2010).
[36] P. Papakonstantinou, J. Margueron, F. Gulminelli, and A. R. Raduta, Phys. Rev. C **88**, 045805 (2013).
[37] T. Fischer, M. Hempel, I. Sagert, Y. Suwa, and J. Schaffner-Bielich, Eur. Phys. J. A **50**, 46 (2014).
[38] T. von Egidy and D. Bucurescu, Phys. Rev. C **72**, 044311 (2005); **73**, 049901 (2006).
[39] S. Typel, G. Röpke, T. Klähn, D. Blaschke, and H. H. Wolter, Phys. Rev. C **81**, 015803 (2010).
[40] S. Furusawa, S. Yamada, K. Sumiyoshi, and H. Suzuki, Astrophys. J. **738**, 178 (2011).
[41] L. Geng, H. Toki, and J. Meng, Prog. Theor. Phys. **113**, 785 (2005).
[42] S. Goriely, M. Samyn, P.-H. Heenen, J. M. Pearson, and F. Tondeur, Phys. Rev. C **66**, 024326 (2002).
[43] N. Chamel, A. F. Fantina, J. M. Pearson, and S. Goriely, Phys. Rev. C **84**, 062802 (2011).
[44] J. M. Pearson, N. Chamel, A. F. Fantina, and S. Goriely, Eur. Phys. J. A **50**, 43 (2014).
[45] A. Y. Potekhin, A. F. Fantina, N. Chamel, J. M. Pearson, and S. Goriely, Astron. Astrophys. **560**, A48 (2013).
[46] J. Duflo and A. P. Zuker, Phys. Rev. C **52**, R23 (1995) [http://amdc.in2p3.fr/web/dz.html].
[47] E. Chabanat *et al.*, Nucl. Phys. A **635**, 231 (1998).
[48] S. Goriely, N. Chamel, and J. M. Pearson, Phys. Rev. C **88**, 024308 (2013).
[49] P. Moller and J. R. Nix, At. Data Nucl. Data Tables **26**, 165 (1981).
[50] P. Moller, J. R. Nix, W. D. Myers, and W. J. Swiatecki, At. Data Nucl. Data Tables **59**, 185 (1995).
[51] G. Audi, M. Wang, A. H. Wapstra, F. G. Kondev, M. MacCormick, X. Xu, and B. Pfeiffer, Chin. Phys. C **36**, 1287 (2012); M. Wang, G. Audi, A. H. Wapstra, F. G. Kondev, M. MacCormick, X. Xu, and B. Pfeiffer, *ibid.* **36**, 1603 (2012) [http://amdc.impcas.ac.cn/evaluation/data2012/data/nubase.mas12].
[52] N. Wang and M. Liu, J. Phys.: Conf. Ser. **420**, 012057 (2013).
[53] J. Dobaczewski, W. Nazarewicz, and T. R. Werner, Phys. Scripta T **56**, 15 (1995).
[54] J. Dobaczewski, W. Nazarewicz, T. R. Werner, J. F. Berger, C. R. Chinn, and J. Decharge, Phys. Rev. C **53**, 2809 (1996).
[55] M. Liebendörfer, Astrophys. J. **633**, 1042 (2005).
[56] R. N. Wolf, D. Beck, K. Blaum, Ch. Böhm, Ch. Borgmann, M. Breitenfeldt, N. Chamel, S. Goriely, F. Herfurth, M. Kowalska, S. Kreim, D. Lunney, V. Manea, E. Minaya Ramirez, S. Naimi, D. Neidherr, M. Rosenbusch, L. Schweikhard, J. Stanja, F. Wienholtz, K. Zuber (ISOLTRAP Collaboration), Phys. Rev. Lett. **110**, 041101 (2013).
[57] S. Kreim, M. Hempel, D. Lunney, and J. Schaffner-Bielich, Int. J. Mass Spectr. **349-350**, 63 (2013).
[58] H. Shen, H. Toki, K. Oyamatsu, and K. Sumiyoshi, Prog. Theor. Phys. **100**, 1013 (1998).
[59] G. M. Fuller and C. J. Smith, Phys. Rev. D **82**, 125017 (2010).
[60] A. Chaudhuri, C. Andreoiu, T. Brunner, U. Chowdhury, S. Ettenauer, A. T. Gallant, G. Gwinner, A. A. Kwiatkowski, A. Lennarz, D. Lunney, T. D. Macdonald, B. E. Schultz, M. C. Simon, V. V. Simon, and J. Dilling, Phys. Rev. C **88**, 054317 (2013).
[61] O. Sorlin and M.-G. Porquet, Phys. Scripta T **152**, 014003 (2013).
[62] J. M. Pearson, R. C. Nayak, and S. Goriely, Phys. Lett. B **387**, 455 (1996).
[63] Q. Zhi, E. Caurier, J. J. Cuenca-Garcia, K. Langanke, G. Martinez-Pinedo, and K. Sieja, Phys. Rev. C **87**, 025803 (2013).
[64] K. Sieja and F. Nowacki, Phys. Rev. C **81**, 061303(R) (2010).
[65] A. F. Fantina *et al.* (unpublished).
[66] L. Coraggio (private communication).